



OPEN

Spatial distribution of elements during osteoarthritis disease progression using synchrotron X-ray fluorescence microscopy

Xiwei Fan¹, Kah Meng Lee², Michael W. M. Jones^{2,3}, Daryl Howard⁴, Antonia Rujia Sun¹, Ross Crawford^{1,5} & Indira Prasadam¹✉

The osteochondral interface is a thin layer that connects hyaline cartilage to subchondral bone. Subcellular elemental distribution can be visualised using synchrotron X-ray fluorescence microscopy (SR-XFM) (1 μm). This study aims to determine the relationship between elemental distribution and osteoarthritis (OA) progression based on disease severity. Using modified Mankin scores, we collected tibia plates from 9 knee OA patients who underwent knee replacement surgery and graded them as intact cartilage (non-OA) or degraded cartilage (OA). We used a tape-assisted system with a silicon nitride sandwich structure to collect fresh-frozen osteochondral sections, and changes in the osteochondral unit were defined using quantified SR-XFM elemental mapping at the Australian synchrotron's XFM beamline. Non-OA osteochondral samples were found to have significantly different zinc (Zn) and calcium (Ca) compositions than OA samples. The tidemark separating noncalcified and calcified cartilage was rich in zinc. Zn levels in OA samples were lower than in non-OA samples ($P = 0.0072$). In OA samples, the tidemark had less Ca than the calcified cartilage zone and subchondral bone plate ($P < 0.0001$). The Zn–strontium (Sr) colocalisation index was higher in OA samples than in non-OA samples. The lead, potassium, phosphate, sulphur, and chloride distributions were not significantly different ($P > 0.05$). In conclusion, SR-XFM analysis revealed spatial elemental distribution at the subcellular level during OA development.

Osteoarthritis (OA) is a chronic degenerative joint condition affecting 528 million individuals worldwide. It is characterised by symptoms such as pain, stiffness, and swelling, and is known to cause significant disability, reduced quality of life, and comorbidities. Despite its widespread occurrence and profound impact on society, the exact causes of OA remain elusive. Therefore, expanding our knowledge of the disease mechanisms and exploring innovative therapeutic approaches to address this significant health challenge is urgently needed.

The osteochondral interface is an essential component in the study of OA progression, as it is increasingly acknowledged as an active remodelling centre in the disease process. This interface is a thin interlayer between the hyaline articular cartilage, which provides a smooth surface for joint movement, and the subchondral bone plate (SBP), a compact bone supporting the cartilage. When examined under a microscope, the osteochondral interface is visible as a layer located between the tidemark (TM) and the cement line^{1–4} (Fig. 1). Within the osteochondral interface, the calcified cartilage zone (CCZ) is a mineralised tissue that plays a crucial role in maintaining joint health. It serves four primary functions in a healthy joint: (1) transmitting mechanical loading, (2) integrating bone and cartilage layers^{5,6}, (3) helping the crosstalk between cartilage and bone^{7,8}, (4) as well as transporting molecules^{9–16}. In biological systems, the synchronisation of elements is indispensable for optimal tissue functioning. In particular, the distribution of mineral elements within the osteochondral interface greatly influences the biomechanical properties of the bone-cartilage unit, allowing for optimal joint function^{2,17,18}. Furthermore, the intricate balance and interplay of different elements contribute significantly to the structural integrity, mechanical properties, cellular activities, and tissue repair processes. For example, Zinc (Zn) and Calcium (Ca) are crucial

¹Centre for Biomedical Technologies, School of Mechanical, Medical and Process Engineering, Queensland University of Technology, 60 Musk Ave/Cnr. Blamey St, Kelvin Grove, QLD 4059, Australia. ²Central Analytical Research Facility, Queensland University of Technology, Brisbane 4059, Australia. ³School of Chemistry and Physics, Queensland University of Technology, Brisbane 4000, Australia. ⁴Australian Synchrotron, Melbourne 3168, Australia. ⁵The Prince Charles Hospital, Brisbane 4032, Australia. ✉email: i.prasadam@qut.edu.au

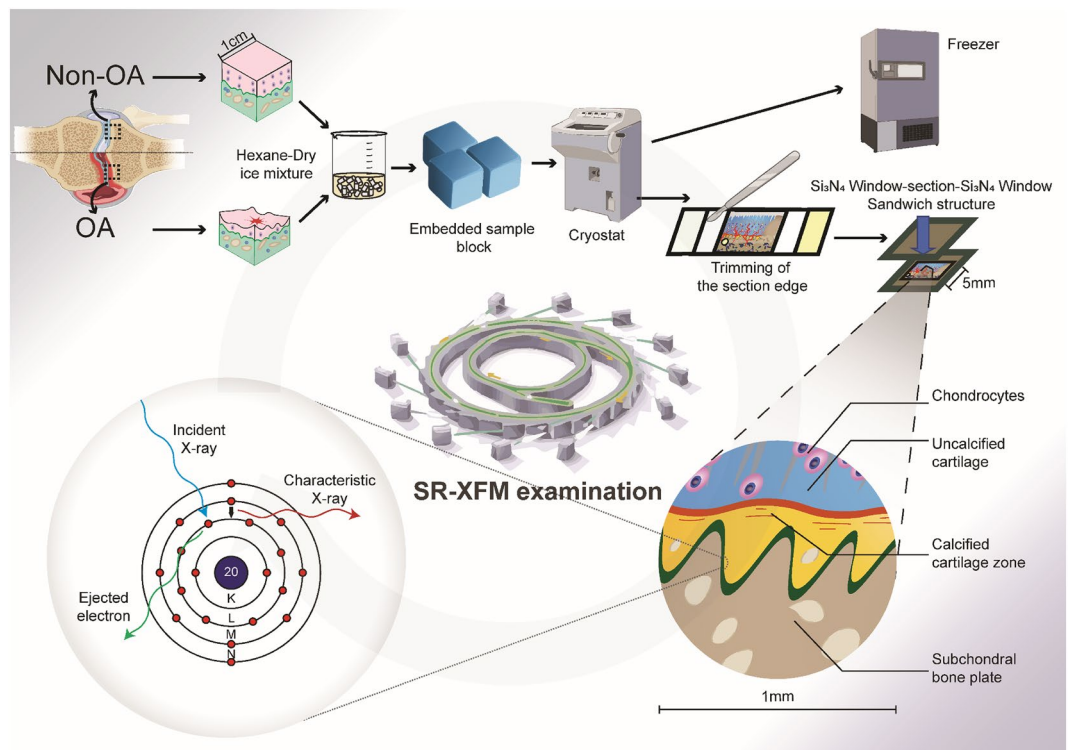


Figure 1. Illustrated workflow to analyse the spatial elemental distribution. Subsequent to collecting samples from total knee replacements, the samples were trimmed into 1 cm × 1 cm × 1 cm blocks utilising the EXAKT bandsaw and were plunge-frozen in a hexane-dry ice mixture. The samples were then embedded with SCEM and completely frozen in a hexane-dry ice mixture. Following the Kawamoto technique, the sample blocks were sectioned, and then medial OA and lateral non-OA sections were collected via a cryofilm tape-assisted system. The cryofilm tapes were subsequently trimmed using a surgical scalpel blade to fit the dimensions of Si₃N₄ windows. Lastly, the sections were embedded in a sandwich structure for SR-XFM analysis, and the figure was generated with BioRender.com.

in maintaining joint stability, preserving mechanical properties, acting as co-factors in signalling pathways, and participating in vital biological activities during pathophysiological processes¹⁹. The element Strontium (Sr) exhibits significant similarities to the chemical attributes of Ca, making it another vital constituent found in the inorganic mineral accumulation at the osteochondral interface²⁰. Potassium (K) contributes to molecular homeostasis through its involvement in membrane potential, electrolyte balance, pH regulation, enzymatic reactions, and cell growth²¹. Magnesium (Mg) and potassium (K) intake has been shown to have disease-modifying effects in OA^{22,23}. Phosphate (P) is essential for bone and CCZ, forming hydroxyapatite and supporting energy metabolism as an ATP component while aiding in nucleic acid and coenzyme synthesis and acid–base balance²⁴. Intra-articular basic calcium phosphate (BCP) crystals, present in most OA joints, are associated with severe degeneration²⁵. Sulphur (S) is pivotal in tissue stability, contributing to amino acids, protein synthesis, redox balance, antioxidant protection, and synthesis of coenzymes and vitamins²⁶. Chloride (Cl) has diverse electrolyte and acid–base balance functions, osmotic pressure regulation, nerve function, and digestion²⁷. Dysfunction of Cl channels in articular cartilage can disrupt the microenvironment, leading to imbalances in the matrix and bone metabolism, partial aseptic inflammation, and progression of OA²⁸. Additionally, certain heavy metals, including lead (Pb) and Cesium (Cs), may impede joint homeostasis through regional deposition^{29,30}. In line with these studies, in our previous studies, we employed EDS and LA-ICP-MS as analytical tools to qualitatively identify the elemental composition in OA disease progression encompassing Ca, P, Sr, oxygen, carbon, K, Mg, Na, and Cl. However, due to the limited sensitivity and lack of spatial analysis to osteochondral interface and quantitative data of EDS and LA-ICP-MS, a more comprehensive investigation is warranted to acquire invaluable insights into the underlying mechanisms of the disease, which could ultimately lead to the development of innovative diagnostic tools and therapeutic strategies.

A range of methods have been devised for visualising the elemental composition and distribution in biological samples, such as Energy-dispersive X-ray spectroscopy (EDS), time-of-flight secondary ion mass spectrometry (TOF-SIMS), and laser ablation inductively coupled plasma mass spectrometry (LA-ICP-MS). These techniques are chosen based on spatial resolution, scanning speed, tissue-specific affinity, and penetration depth. Among different available methods, synchrotron X-ray fluorescence microscopy (SR-XFM) offers subcellular spatial resolution (with an effective pixel size of 1.0 μm depending on various parameters). It is a non-destructive method capable of imaging large tissue areas (mm²) with adequate penetration depth and minimal tissue preparation^{31,32}. Despite its advantages, SR-XFM has not been used to study the endogenous distribution changes of osteochondral

interface elements during OA due to challenges in preparing chemical-free fresh-frozen sections. Prior studies^{33,34} have employed resin-embedded samples for SR-XFM preparation, but the formalin or ethanol fixation during this process may alter the endogenous elemental distribution in cells³⁵, soft tissues³⁶, and hard tissues³⁷; consequently, this could introduce bias and present an inaccurate picture of elemental distribution during disease progression³⁸. To accurately examine endogenous changes, we developed a tape-assisted system that accommodated fresh-frozen tissue for SR-XFM³⁹ and implemented a three-stage approach to improve data accuracy and value, which involved enhancements in sample preparation, image acquisition, and signal processing. This research aims to provide a comprehensive understanding of the spatial distribution and potential variations of elements within the osteochondral interface during OA progression. Specifically, we have chosen to analyse the spatial distribution of Zn, Ca, Sr, Pb, K, P, S, Cl and Cs based on our previous studies because of their role in cartilage and joint homeostasis. The utilization of synchrotron X-ray fluorescence microscopy (SR-XFM) will enable a more detailed analysis, offering valuable insights into the underlying mechanisms of OA and paving the way for the development of innovative diagnostic tools and therapeutic strategies.

Results

In order to examine the distribution patterns of elements in osteochondral tissues classified by the severity of the disease, we assessed the presence of Zn, Ca, Sr, Pb, K, P, S, Cl, and Cs in nine patient-matched osteochondral tissue sections based on the previous LA-ICP-MS and EDS results from our research group⁴⁰, adhering to the process illustrated in (Fig. 1). The detailed modified Mankin score comparison is shown in Table 1.

Spatial distribution of Zn during OA progression. First, Zn accumulation was stratigraphically localised in the non-OA samples in the osteochondral junction. The TM region of the non-OA sample showed a strong Zn accumulation signal, followed by the SBP zone and CCZ zone (Fig. 2A,B). Quantitatively, Zn abundance for the non-OA for TM, CCZ, and SBP is $1210.70 \pm 284.61.97$ ng/cm², 267.88 ± 53.85 ng/cm², and 332.39 ± 54.82 ng/cm², respectively. Additionally, the cement line, which is the region between SBP and CCZ, has a distinct high Zn-rich contour in non-OA samples. We noticed an intriguing high Zn accumulation in the chondrocyte lacunae in the non-OA CCZ region. In terms of osteochondral junction stratigraphy for OA, Zn localisation was more prevalent in TM, with Zn levels in OA samples being comparable between CCZ and SBP. Quantitatively, Zn abundance for OA TM, CCZ, and SBP is 919.45 ± 128.93 ng/cm², 292.30 ± 42.11 ng/cm², and 321.51 ± 53.03 ng/cm², respectively. When comparing non-OA and OA samples, Zn is more abundant and wavier in the non-OA samples than in the OA sample in the TM area ($P = 0.0072$). Zinc follows the TM contour, and we found the zinc tortuosity index is increased in the OA sample ($P < 0.0001$, Fig. 2C). However, no difference was observed between CCZ and SBP when comparing non-OA and OA samples ($P > 0.05$, Fig. 3A–D).

Spatial distribution of Ca during OA progression. The Ca abundance varies depending on the osteochondral stratigraphy, similar to Zn. Both non-OA and OA samples' CCZ and SBP contain the same abundance of Ca (Fig. 2A,B). We observed an even Ca distribution throughout the non-OA TM with no distinction between TM, CCZ, and SBP observed. Quantitatively, the Ca abundance for non-OA TM, CCZ and SBP are 426.24 ± 134.08 µg/cm², 447.57 ± 121.97 µg/cm², and 438.46 ± 120.59 µg/cm², respectively. The Ca content of OA TM is lower than that of OA CCZ and OA SBP ($P < 0.0001$ for both). In OA samples, we found no statistical difference in CCZ and SBP ($P > 0.05$). Quantitatively, the Ca abundance for OA TM, CCZ, and SBP is 389.44 ± 51.74 µg/cm², 474.71 ± 63.35 µg/cm², and 455.821 ± 58.05 µg/cm², respectively. No statistical change was observed in TM, CCZ and SBP when comparing Ca abundance in patient-matched samples between the non-OA and OA counterparts ($P > 0.05$, Fig. 4A–D).

Sr distribution changes during OA progression. Sr follows a similar distribution pattern as Ca (Fig. 2A,B). The Sr abundance for non-OA TM, CCZ, and SBP is 199.41 ± 43.77 ng/cm², 203.41 ± 41.30 ng/cm², and 188.75 ± 45.21 ng/cm², respectively. In non-OA samples, Sr distribution is lower in the SBP region compared with the TM ($P = 0.0042$) and the CCZ ($P = 0.0132$). The Sr abundance for OA TM, CCZ, and SBP is 186.87 ± 11.83 ng/cm², 206.67 ± 13.33 ng/cm², and 192.31 ± 12.77 ng/cm², respectively. In OA samples, CCZ shows higher abundance compared with the TM ($P = 0.0023$) and SBP ($P = 0.0017$). When comparing non-OA and OA samples, the Sr abundance shows no statistical changes between the non-OA and OA counterparts ($P > 0.05$, Fig. 5A–D).

	Non-OA	OA
Cartilage structure	1.96 ± 0.87	5.26 ± 0.54
Cellularity	0.95 ± 0.63	4.95 ± 0.98
Proteoglycan depletion	0.68 ± 0.73	1.91 ± 0.75
Tidemark integrity	–	0.99 ± 0.63
Total Mankin score	3.59 ± 0.66	13.13 ± 0.66

Table 1. Modified Mankin score comparison.

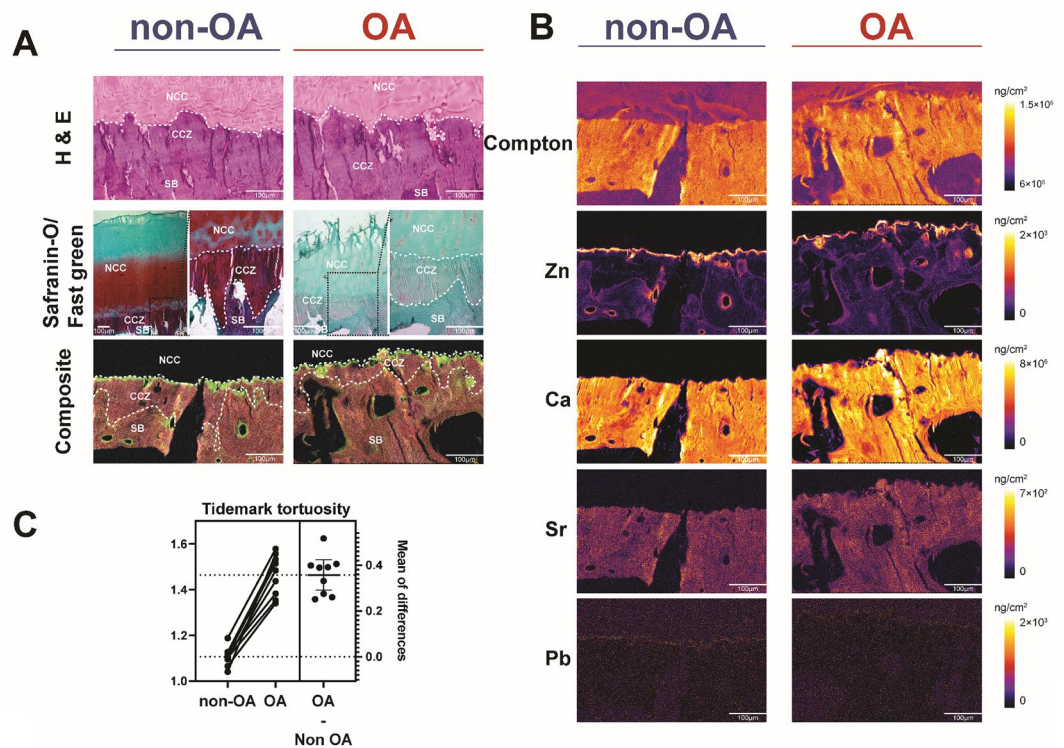


Figure 2. Elemental mapping of non-OA and OA osteochondral interface. **(A)** Representative elemental mapping of structural changes between non-OA and OA osteochondral interface. Figures are representative of $n = 9$ patient-matched samples. **(B)** Quantitative elemental osteochondral interface heatmaps in OA tissues graded according to disease severity. Representative Zn, Ca, Sr, and Pb elemental mapping of quantitative changes between non-OA and OA osteochondral interface. Figures are representative of $n = 9$ patient-matched samples. Scale bar: $100 \mu\text{m}$. **(C)** Quantitation of the tidemark tortuosity index (length of the upper and bottom contour of tidemark from the starting to the endpoint). NCC Noncalcified cartilage, CCZ Calcified cartilage zone, SBP Subchondral bone plate, TM Tidemark. ($n = 9$, paired two-tailed t-test, data was presented as ng/cm^2).

Pb distribution changes during OA progression. In terms of Pb distribution, we found Pb accumulation in the TM region (Fig. 2A,B), consistent with previous research³⁴. The Pb abundance for non-OA TM, CCZ, and SBP is $659.35 \pm 46.60 \text{ ng}/\text{cm}^2$, $530.41 \pm 42.67 \text{ ng}/\text{cm}^2$, and $523.41 \pm 45.22 \text{ ng}/\text{cm}^2$, respectively. The abundance of Pb was higher in TM than the SBP in both non-OA ($P < 0.0001$). Non-OA CCZ showed higher Pb abundance than non-OA SBP ($P = 0.0287$). The Pb abundance for OA TM, CCZ, and SBP is $602.39 \pm 54.50 \text{ ng}/\text{cm}^2$, $509.99 \pm 45.04 \text{ ng}/\text{cm}^2$, and $495.40 \pm 42.45 \text{ ng}/\text{cm}^2$, respectively. OA TM shows higher Pb abundance compared with SBP ($P < 0.0001$). When comparing non-OA and OA samples, the Pb abundance shows no statistical changes ($P > 0.05$, Fig. 6A–D).

We found no statistical difference in the spatial distribution of other elements, such as K, P, S, and Cl, between non-OA and OA samples ($P > 0.05$). The phenomenon is due to XFM's inherent higher sensitivity for metal elements, particularly from Titanium to Uranium, but lower sensitivity for lighter elements (Fig. S1).

Colocalisation of elements during OA progression. Next, we used colocalisation analysis to reveal the co-distribution changes of elements during OA progression. The results showed that Ca–Sr, Ca–Zn, and Zn–Sr colocalisation index is higher in TM than CCZ and SBP in both non-OA and OA samples ($P_{\text{Ca-Sr}} = 0.032$; $P_{\text{Ca-Zn}} = 0.001 <$; $P_{\text{Zn-Sr}} = 0.00151$, Figs. S2–S4). OA Zn–Sr in the TM has a higher slope than non-OA ($P = 0.015 < 0.05$, Fig. S4). In both non-OA and OA samples, the Pb–Sr colocalisation index was higher in TM than CCZ and SBP ($P = 0.017 < 0.05$, Fig. S5), while no correlation was found between Ca–Pb samples ($P > 0.05$, Fig. S6). No correlation was found between Zn–Pb in both non-OA and OA samples ($P > 0.05$, Fig. S7).

Discussion

To our knowledge, this is the first paper that reports changes in the stratigraphy and disease-specific differences of elements in OA graded according to disease severity, in which the lateral side is healthy, and the medial side is damaged based on modified Mankin score system at a subcellular resolution ($1 \mu\text{m}$)^{33,34}.

In the present work, we found that unique spatial patterns of element distribution exist at the osteochondral interface. According to statistical analyses, non-OA osteochondral samples differ significantly from OA osteochondral samples in their elemental compositions, especially for Zn, Ca, and Pb. The TM separating the calcified cartilage from the noncalcified cartilage showed a significant Zn level. Unexpectedly, the Zn content of the OA

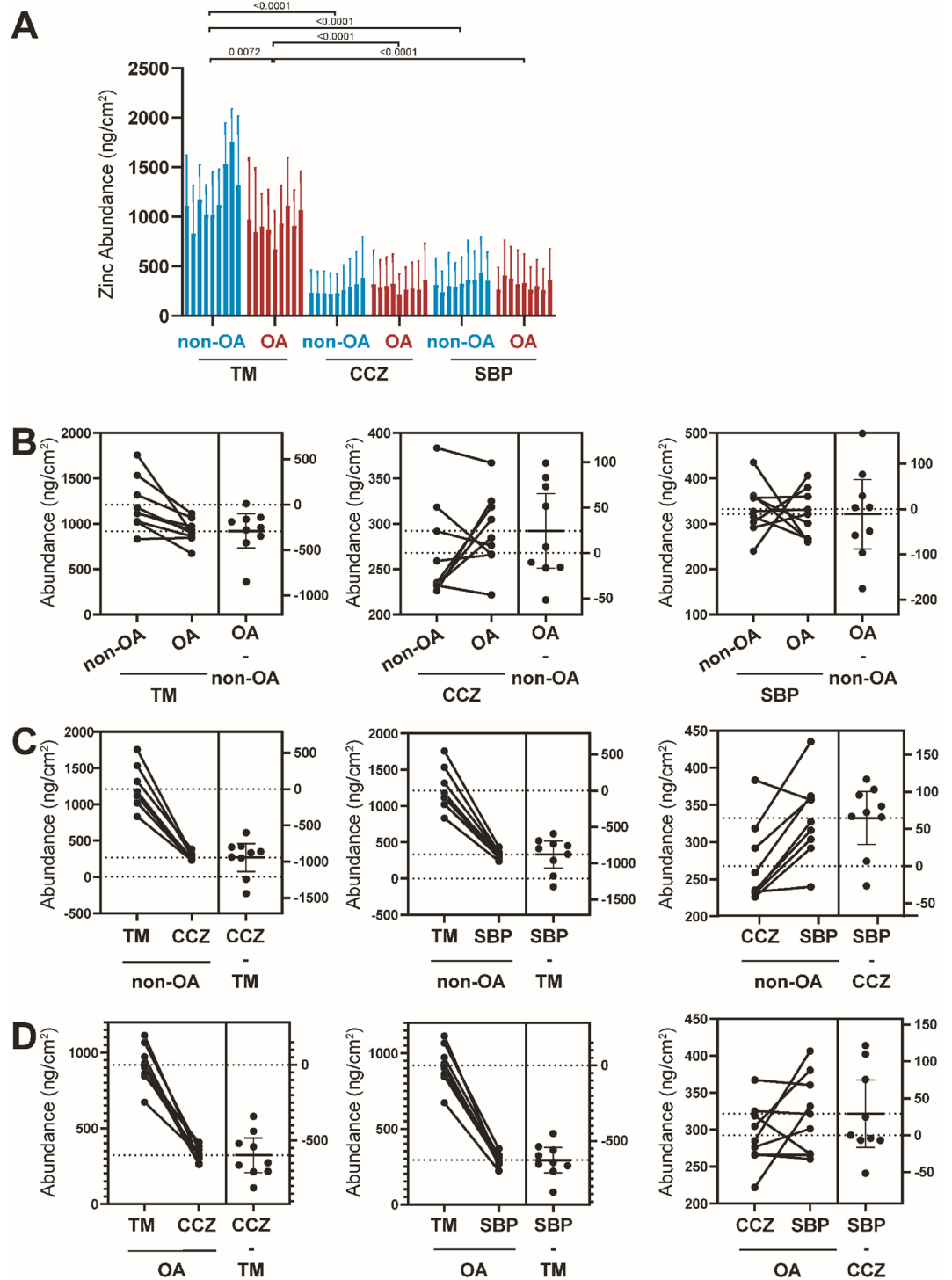
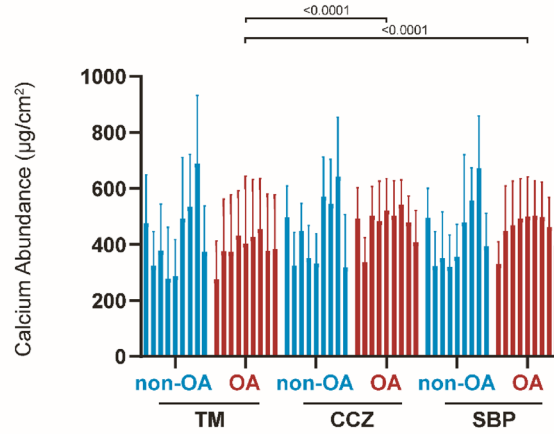
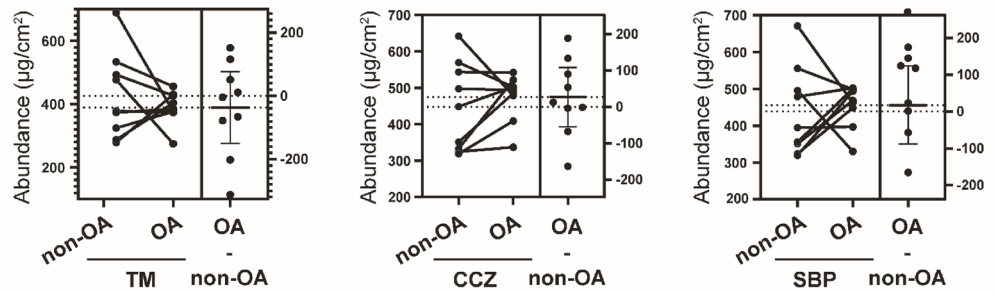


Figure 3. Quantitative Zn elemental changes of osteochondral interface graded according to disease severity. (A) The bar graph shows the Zn abundance using the technical replicates for each pixel derived from the region of interest (ROI) in individual specimens from non-OA and OA osteochondral sections. Values are expressed as Mean \pm SD (data were gathered from each pixel including each region of interest, paired two-tailed t-test, data was presented as ng/cm²). (B) Paired T-test to compare group-wise differences in OA samples compared with non-OA samples. (C) Paired T-test to compare group-wise differences according to stratigraphy in non-OA samples. (D) Paired T-test to compare group-wise differences according to stratigraphy in OA samples. Figures are representative of n = 9 patient-matched samples. *TM* Tidemark, *CCZ* Calcified cartilage zone, *SBP* Subchondral bone plate. Values are expressed as Mean \pm SD (n = 9, paired two-tailed t-test, data was presented as ng/cm²).

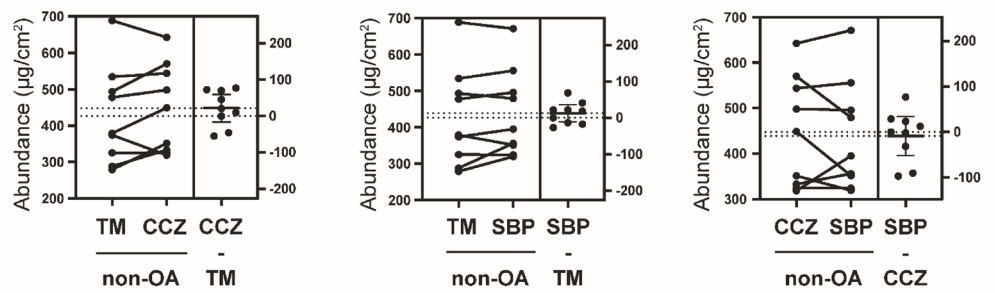
A



B



C



D

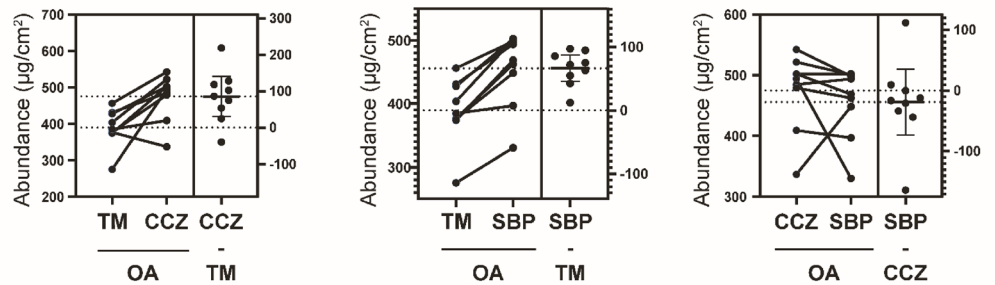


Figure 4. Quantitative Ca elemental changes of osteochondral interface graded according to disease severity. (A) The bar graph shows the Ca abundance using the technical replicates for each pixel derived from the region of interest (ROI) in individual specimens from non-OA and OA osteochondral sections. Values are expressed as Mean \pm SD (data were gathered from each pixel including each region of interest, paired two-tailed t-test, data was presented as $\mu\text{g}/\text{cm}^2$). (B) Paired T-test to compare group-wise differences in OA samples compared with non-OA samples. (C) Paired T-test to compare group-wise differences according to stratigraphy in non-OA samples. (D) Paired T-test to compare group-wise differences according to stratigraphy in OA samples. Figures are representative of $n = 9$ patient-matched samples. *TM* Tidemark, *CCZ* Calcified cartilage zone, *SBP* Subchondral bone plate. Values are expressed as Mean \pm SD ($n = 9$, paired two-tailed t-test, data was presented as $\mu\text{g}/\text{cm}^2$).

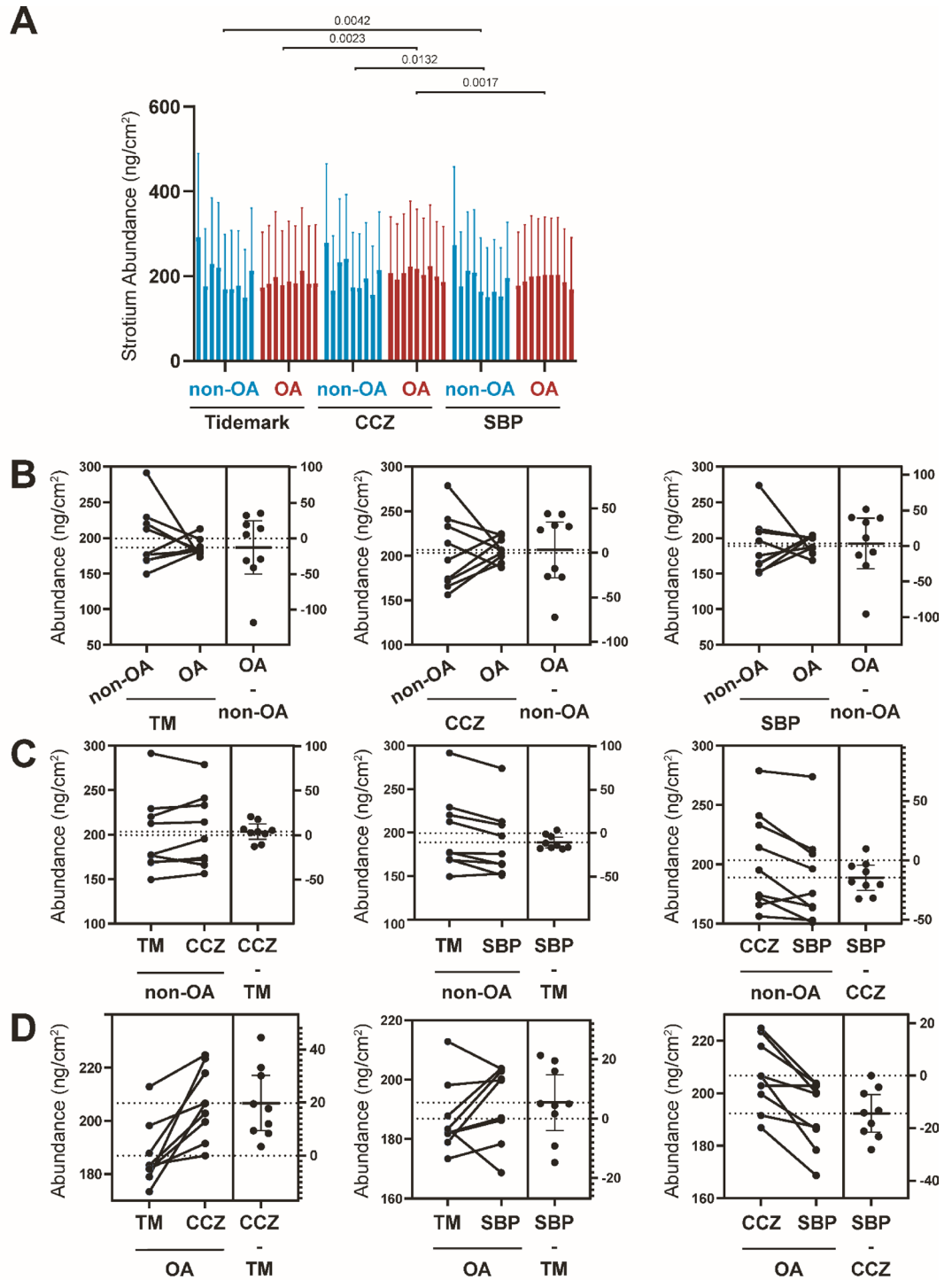


Figure 5. Quantitative Sr elemental changes of osteochondral interface graded according to disease severity. (A) The bar graph shows the Sr abundance using the technical replicates for each pixel derived from the region of interest (ROI) in individual specimens from non-OA and OA osteochondral sections. Values are expressed as Mean \pm SD (data were gathered from each pixel including each region of interest, paired two-tailed t-test, data was presented as ng/cm²). (B) Paired T-test to compare group-wise differences in OA samples compared with non-OA samples. (C) Paired T-test to compare group-wise differences according to stratigraphy in non-OA samples. (D) Paired T-test to compare group-wise differences according to stratigraphy in OA samples. Figures are representative of n = 9 patient-matched samples. *TM* Tidemark, *CCZ* Calcified cartilage zone, *SBP* Subchondral bone plate. Values are expressed as Mean \pm SD (n = 9, paired two-tailed t-test, data was presented as ng/cm²).

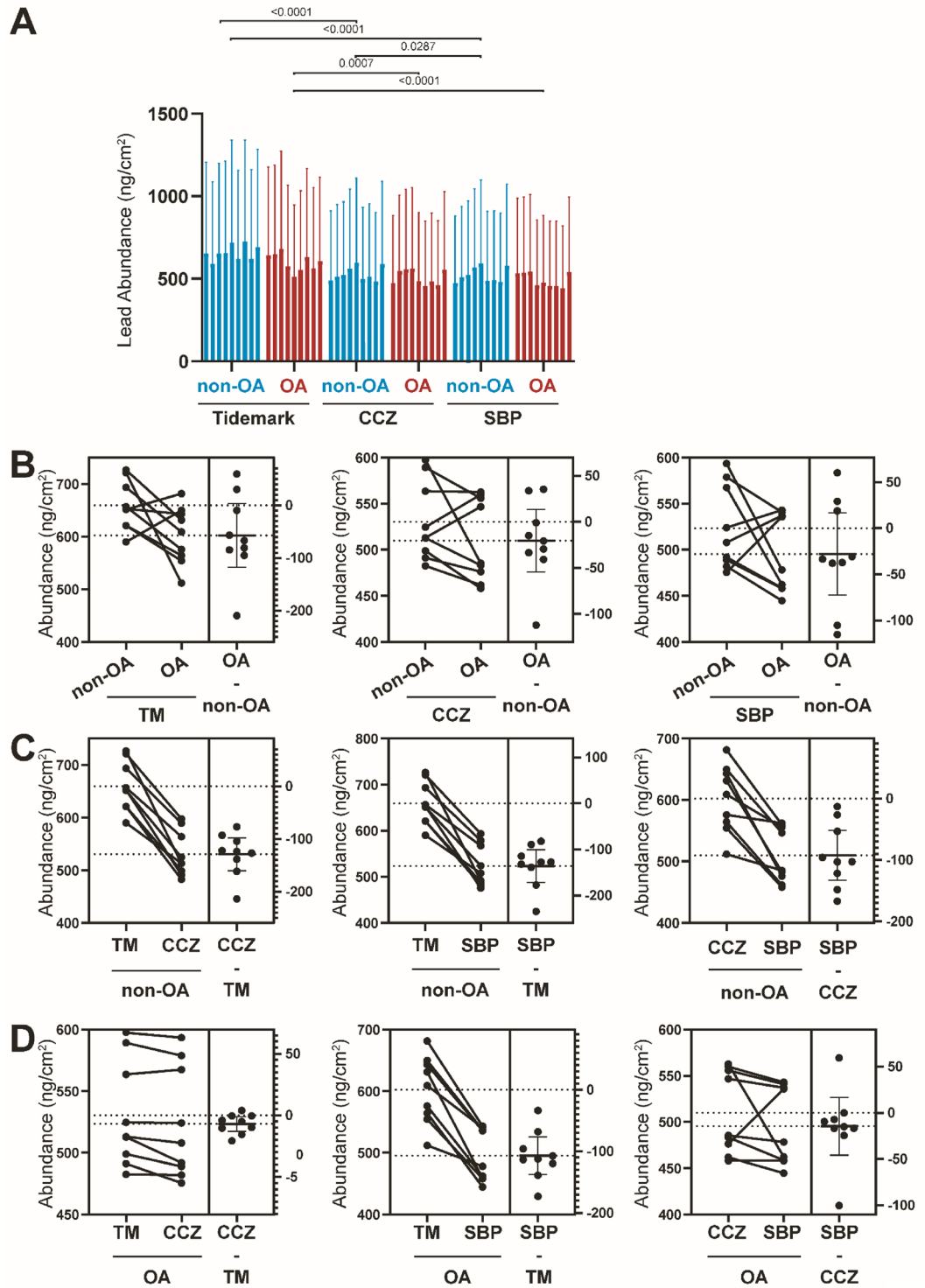


Figure 6. Quantitative Pb elemental changes of osteochondral interface graded according to disease severity. (A) The bar graph shows the Pb abundance using the technical replicates for each pixel derived from the region of interest (ROI) in individual specimens from non-OA and OA osteochondral sections. Values are expressed as Mean \pm SD (data were gathered from each pixel including each region of interest, paired two-tailed t-test, data was presented as ng/cm²). (B) Paired T-test to compare group-wise differences in OA samples compared with non-OA samples. (C) Paired T-test to compare group-wise differences according to stratigraphy in non-OA samples. (D) Paired T-test to compare group-wise differences according to stratigraphy in OA samples. Figures are representative of n = 9 patient-matched samples. *TM* Tidemark, *CCZ* Calcified cartilage zone, *SBP* Subchondral bone plate. Values are expressed as Mean \pm SD (n = 9, paired two-tailed t-test, data was presented as ng/cm²).

TM was lower than that of the NON-OA TM ($P = 0.0072$). Additionally, we discovered less Ca in the TM in the OA samples than in the subchondral bone plate and calcified cartilage zone ($P < 0.0001$ for both). The Zn-Sr colocalisation index was higher in the OA TM region than in the non-OA samples.

TM has traditionally been regarded as a remnant of the growth plate during secondary ossification. Prior studies have identified alterations in the TM, such as increased tortuosity index, TM duplication, and endochondral ossification occurring during the progression of OA^{40,41}. These changes have been linked to the redifferentiation of chondrocytes in the CCZ⁴². Discontinuity of the TM at the osteochondral interface has also been observed during OA progression^{40,41,43,44}. However, these studies mainly provided descriptive analyses without quantitative data. Our findings suggest that in non-OA samples, TM discontinuity is closely associated with an uneven distribution of Zn in the TM region. Additionally, a higher Zn-Sr colocalisation index indicates a distinct regional variation in Zn distribution.

We also noticed a substantial change in Zn abundance and distribution in the TM area between non-OA and OA samples. Additionally, we found that the tortuosity index, shaped by Zn, is significantly increased (Fig. 2A). An increase in TM tortuosity is a characteristic identified through Safranin-O/fast green staining and is often associated with the reactivation of endochondral calcification and bone remodelling^{40,44}. During biological processes, Zn interacts with various enzymes, such as alkaline phosphatase (ALP) and matrix metalloproteinases (MMPs), and serves as an essential trace element in numerous enzymes' reactive cores, contributing to healthy skeletal growth⁴⁵. Although the precise role of Zn in bone metabolism remains unclear, recent studies suggest that it promotes bone formation by enhancing osteoblastic cell proliferation⁴⁶. Conversely, research on Zn-deficient rats found no differences in bone mineral density, turnover, architecture, or biomechanics compared to control subjects⁴⁷. In light of these findings, we employed laser microdissection microscopy for proteomics identification in the CCZ and identified several Zn-related proteins, including superoxide dismutase (SOD1), S100 calcium-binding protein A7 (S100A7), ALP, and others⁴⁰. The Zn change could also be related to crystal formation change, as researchers found a higher mineral crystal thickness in the lateral compartment of OA⁴⁸. However, no evidence exists that the Zn contributed to the crystal growth at this stage; further study is needed to elucidate the specific mechanism behind Zn accumulation in the TM.

This research also discovered a higher concentration of Ca in the CCZ of OA joints compared to the TM. The CCZ is an area of active remodelling during OA progression. Earlier studies have shown that the thickness of both the CCZ and the SBP undergoes dynamic changes during OA development^{40,44}. In the early stages, CCZ thickness increases while SBP thickness decreases, but this reverses in later stages. These thickness fluctuations lead to active mineral changes within the CCZ and SBP. The exact role of abnormal mineralisation in the interaction between CCZ and SBP is still unclear. Additionally, it is well-established that collagen fibres and mineralisation determine the stiffness of the CCZ and SBP⁴⁰. Our previous research found a reduction in the elastic modulus of both the CCZ and SBP, but the present study did not find any significant differences in Ca levels⁴⁰. This discrepancy may be due to the combined effects of collagen bundles and the mineralisation process on the elastic modulus of the samples. A prior study reported increased stiffness in the collagen fibres of osteoarthritic cartilage, which could explain the observed changes in the elastic modulus⁴⁹. As OA progresses, the reorganisation and entanglement of collagen fibres inevitably lead to a decrease in the elastic modulus.

Blood Pb levels are commonly recognised as a risk factor for knee OA²⁹. However, the impact of regionally deposited Pb on OA progression is poorly understood. We discovered Pb accumulation in the deeper layers of the TM (TM). It is important to note that the process of Ca^{2+} being replaced by Pb^{2+} in Ca-hydroxyapatite is well-established at high Pb concentrations and is expected to occur similarly at low concentrations⁵⁰. However, our study revealed that Pb does not have the same distribution as Ca, as it exhibits a higher affinity for the TM area, which is consistent with prior reports^{33,34}. Earlier studies have suggested that Pb accumulation may contribute to disease progression^{33,34}. However, we found no correlation between Pb and other elements in the osteochondral interface, nor between non-OA and OA samples. Our patients were recruited from Brisbane in Australia, a city with a consistently good air quality index (PM 2.5 ranging from 10 to 30). This low exposure to Pb might explain why it does not reach a level that can influence or accelerate OA progression. Future studies analysing local Pb accumulation in the tidemark and its relation to OA progression may help clarify the association.

There are some limitations to the current study. All the samples were collected from OA patients undergoing knee replacement surgery. Therefore, some changes may be overlooked or underestimated compared to normal samples without the signs of OA. The stratification of the non-OA and OA samples could omit the dynamic changes in the moderate OA stage, which will be investigated in future studies. Another limitation is that different elements hold different thresholds when performing quantitative XFM⁵¹. Therefore, some light elements have lower sensitivity, so we cannot measure the difference. However, this does not mean there is no difference between different groups.

This study presents novel findings regarding the changes in stratigraphy and disease-specific differences of osteoarthritis (OA) elements at a subcellular resolution. We observed unique spatial patterns of element distribution at the osteochondral interface and significant differences in elemental compositions between non-OA and OA osteochondral samples, highlighting the significance of elemental distribution in OA pathogenesis.

Methods

Human ethics and sample preparation. All methods were performed in accordance with guidelines and regulations, which were approved by the ethics committee of the Queensland University of Technology (Human ethics number: #1400001024). Nine participants provided written informed consent to donate the tissues for the knee arthroplasty surgery. After the surgery, the medial and lateral bearing surfaces of the tibia plates of the human donors were collected from St Vincent's Private Hospital. Based on the Modified Mankin scoring system⁵², the samples from each patient were matched and graded as non-OA (Grade 0–1) and OA (Grade 4)

samples by three blinded observers, in which non-OA is the relatively intact knee joint with cartilage and SBP. In contrast, OA contains degraded cartilage and SBP sclerosis (Detailed demographic data is shown in Table S1). Patients with inflammatory bone diseases were excluded from the study. Patients with a previous medical history, bisphosphonate, and other medication therapy that could contribute to bone and cartilage metabolism and the elemental change were also excluded. EXAKT 310 Diamond Band Saw (EXAKT Apparatebau GmbH & Co. KG; Norderstedt, Germany) was used to cut off the intact and lesion part of the cartilage, and 1 cm × 1 cm × 1 cm cubes were trimmed. We plunge-froze samples in a hexane-dry ice mixture which were then embedded in the super cryo embedding medium (SCEM) (SECTION-LAB, Japan) and froze completely in the hexane-dry ice mixture using the Kawamoto technique⁵³.

Sectioning. Following our previously published protocol³⁹, we sectioned all samples at 10 μm thickness using a CryoStar NX70 cryostat (ThermoFisher Scientific, USA) with a tungsten carbide knife, D profile (Dorn & Hart Microedge, USA). Then, since better sections were produced at a lower temperature⁵⁴, we set the specimen at −30 °C and the knife at −28 °C. After that, we attached the tissue to Kawamoto's cryofilm tapes (3C(16UF), SECTION-LAB, Japan) to support the tissue and cut blocks into 5 mm × 5 mm pieces. We flipped over the tape (with sections on top) and mounted them on a Si₃N₄ window (600 nm thick; Australian National Fabrication Facility, QLD, Australia) with the matching tissue face exposed for analysis. After that, we freeze-dried the windows and stored them at room temperature in a sealed container to avoid protein degradation. We randomly positioned the samples in the frame by an observer-blind method to avoid selection bias.

X-ray fluorescence microscopy image quantification. Prior to the beamtime, we mapped to identify the osteochondral interface using optical and fluorescence mosaic of the windows obtained using both Olympus VS120 Slide scanner and Zeiss LSM 710 Confocal Laser Scanning/Multi-photon Microscope with OlyVIA 2.9 software. Fluorescent mapping was undertaken at ~15 keV, with 5 mm × 5 mm areas mapped per sample at low resolution. We selected representative regions of interest with 1 mm × 1 mm size from these mappings. Next, we scanned these regions at high resolution and high sensitivity at parameters to achieve the best possible elemental maps. XFM photons were gathered at the Australian Synchrotron's XFM beamline as an event mode data stream⁵⁵ using the Maia detector system⁵⁶ and processed using the dynamic analysis method⁵⁷ as implemented in GeoPIXE⁵⁸. The data were quantified using well-characterised metallic foils and exported as 32-bit tiffs with units in areal density (ng/cm²). The tortuosity index was described as the ratio of the meandering curve to the straight-line length between the endpoints⁵⁹.

Colocalisation analysis. Following the previously published protocol⁶⁰, we measured Zn, Ca, Pb, and Sr elemental mappings using colocalisation analysis as Pearson's *r*, Costes' regression threshold, and Mander's overlap coefficients, performed in Fiji using the 'Coloc 2' plugin.

Statistical analysis. GraphPad Prism 8 (San Diego, USA) software was used to compute statistical analysis. They grouped experimental replicate data from each group and calculated the mean values at the sample level for further statistical comparison. A Shapiro–Wilk test was performed to assess the normality of the data, and all tested data groups passed this test successfully. After that, a paired t-test was conducted, and statistical significance was defined as p-values less than 0.05 for the above procedures. The researchers reported all data as mean values along with their standard deviation (SD).

Data availability

The manuscript contains all the necessary data. Any remaining information can be obtained from the corresponding author upon reasonable request.

Received: 15 January 2023; Accepted: 12 June 2023

Published online: 23 June 2023

References

- Deng, B. *et al.* Quantitative study on morphology of calcified cartilage zone in OARSI 0~4 cartilage from osteoarthritic knees. *Curr. Res. Transl. Med.* **64**(3), 149–154. <https://doi.org/10.1016/j.retram.2016.01.009> (2016).
- Zhang, Y. *et al.* Analysis of the mineral composition of the human calcified cartilage zone. *Int. J. Med. Sci.* **9**(5), 353–360. <https://doi.org/10.7150/ijms.4276> (2012).
- Wang, F., Yang, L., Duan, X., Tan, H. & Dai, G. Study on shape and structure of calcified cartilage zone in normal human knee joint. *Zhongguo Xiu Fu Chong Jian Wai Ke Za Zhi* **22**(5), 524–527 (2008).
- Wang, F. *et al.* Histomorphometric analysis of adult articular calcified cartilage zone. *J. Struct. Biol.* **168**(3), 359–365. <https://doi.org/10.1016/j.jsb.2009.08.010> (2009).
- Meachim, G. & Bentley, G. Horizontal splitting in patellar articular cartilage. *Arthritis Rheum.* **21**(6), 669–674. <https://doi.org/10.1002/art.1780210610> (1978).
- Matthewson, M. H. & Dandy, D. J. Osteochondral fractures of the lateral femoral condyle: A result of indirect violence to the knee. *J. Bone Joint Surg.* **60**(2), 199–202 (1978).
- Fan, X., Wu, X., Crawford, R., Xiao, Y. & Prasad, I. Macro, micro, and molecular: Changes of the osteochondral interface in osteoarthritis development. *Front. Cell Dev. Biol.* **9**, 1148. <https://doi.org/10.3389/fcell.2021.659654> (2021).
- Prasad, I. *Cross-talk of Subchondral Bone Osteoblasts and Articular Cartilage Chondrocytes: A New Insight in Understanding Osteoarthritis Pathogenesis* (Queensland University of Technology, 2009).
- Maroudas, A., Bullough, P., Swanson, S. A. & Freeman, M. A. The permeability of articular cartilage. *J. Bone Joint Surg.* **50**(1), 166–177 (1968).

10. Honner, R. & Thompson, R. C. The nutritional pathways of articular cartilage: An autoradiographic study in rabbits using 35S injected intravenously. *J. Bone Joint Surg.* **53**(4), 742–748 (1971).
11. Brower, T. D., Akahoshi, Y. & Orlic, P. The diffusion of dyes through articular cartilage in vivo. *J. Bone Joint Surg.* **44**(3), 456–463 (1962).
12. Ogata, K. & Whiteside, L. A. Barrier to material transfer at the bone-cartilage interface: Measurement with hydrogen gas in vivo. *Clin. Orthop. Relat. Res.* **145**, 273–276 (1979).
13. Collins, D. H. *The Pathology of Articular and Spinal Diseases* (Edward Arnold, 1949).
14. Berry, J. L., Thaler-Oberdoerster, D. A. & Greenwald, A. S. Subchondral pathways to the superior surface of the human talus. *Foot Ankle* **7**(1), 2–9 (1986).
15. Imhof, H., Breitenseher, M., Kainberger, F., Rand, T. & Trattnig, S. Importance of subchondral bone to articular cartilage in health and disease. *Top. Magn. Reson. Imaging* **10**(3), 180–192 (1999).
16. Lyons, T. J., McClure, S. F., Stoddart, R. W. & McClure, J. The normal human chondro-osseous junctional region: Evidence for contact of uncalcified cartilage with subchondral bone and marrow spaces. *BMC Musculoskelet. Disord.* **7**, 52. <https://doi.org/10.1186/1471-2474-7-52> (2006).
17. Duer, M. J., Frisci, T., Murray, R. C., Reid, D. G. & Wise, E. R. The mineral phase of calcified cartilage: Its molecular structure and interface with the organic matrix. *Biophys. J.* **96**(8), 3372–3378. <https://doi.org/10.1016/j.bpj.2008.12.3954> (2009).
18. Lee, J. Y. *et al.* Relationship of bone mineral density to progression of knee osteoarthritis. *Arthritis Rheum.* **65**(6), 1541–1546. <https://doi.org/10.1002/art.37926> (2013).
19. Jomova, K. *et al.* Essential metals in health and disease. *Chem. Biol. Interact.* **367**, 110173. <https://doi.org/10.1016/j.cbi.2022.110173> (2022).
20. Niu, Y., Du, T. & Liu, Y. Biomechanical characteristics and analysis approaches of bone and bone substitute materials. *J. Funct. Biomater.* **14**(4), 212. <https://doi.org/10.3390/jfb14040212> (2023).
21. Udensi, U. K. & Tchounwou, P. B. Potassium homeostasis, oxidative stress, and human disease. *Int. J. Clin. Exp. Physiol.* **4**(3), 111–122. https://doi.org/10.4103/ijcep.ijcep_43_17 (2017).
22. Qin, B. *et al.* Association of dietary magnesium intake with radiographic knee osteoarthritis: Results from a population-based study. *Arthritis Care Res.* **64**(9), 1306–1311. <https://doi.org/10.1002/acr.21708> (2012).
23. Zhang, Y. *et al.* Associations of dietary macroelements with knee joint structures, symptoms, quality of life, and comorbid conditions in people with symptomatic knee osteoarthritis. *Nutrients* **14**(17), 3576. <https://doi.org/10.3390/nu14173576> (2022).
24. Chande, S. & Bergwitz, C. Role of phosphate sensing in bone and mineral metabolism. *Nat. Rev. Endocrinol.* **14**(11), 637–655. <https://doi.org/10.1038/s41574-018-0076-3> (2018).
25. Corr, E. M., Cunningham, C. C., Helbert, L., McCarthy, G. M. & Dunne, A. Osteoarthritis-associated basic calcium phosphate crystals activate membrane proximal kinases in human innate immune cells. *Arthritis Res. Ther.* **19**(1), 23. <https://doi.org/10.1186/s13075-017-1225-0> (2017).
26. Townsend, D. M., Tew, K. D. & Tapiero, H. Sulfur containing amino acids and human disease. *Biomed. Pharmacother.* **58**(1), 47–55. <https://doi.org/10.1016/j.biopha.2003.11.005> (2004).
27. Turck, D. *et al.* Dietary reference values for chloride. *Efsa J.* **17**(9), e05779. <https://doi.org/10.2903/j.efsa.2019.5779> (2019).
28. Lin, Z. *et al.* Chloride channel and inflammation-mediated pathogenesis of osteoarthritis. *J. Inflamm. Res.* **15**, 953–964. <https://doi.org/10.2147/jir.S350432> (2022).
29. Nelson, A. E. *et al.* Whole blood lead levels are associated with radiographic and symptomatic knee osteoarthritis: A cross-sectional analysis in the Johnston County Osteoarthritis Project. *Arthritis Res. Ther.* **13**(2), R37. <https://doi.org/10.1186/ar3270> (2011).
30. Collin, M. S. *et al.* Bioaccumulation of lead (Pb) and its effects on human: A review. *J. Hazard. Mater. Adv.* **7**, 100094. <https://doi.org/10.1016/j.hazadv.2022.100094> (2022).
31. Jones, M. W. M., Hare, D. J., James, S. A., de Jonge, M. D. & McColl, G. Radiation dose limits for bioanalytical X-ray fluorescence microscopy. *Anal. Chem.* **89**(22), 12168–12175. <https://doi.org/10.1021/acs.analchem.7b02817> (2017).
32. Hare, D. J. *et al.* High-resolution complementary chemical imaging of bio-elements in *Caenorhabditis elegans*. *Metallomics* **8**(2), 156–160. <https://doi.org/10.1039/c5mt00288e> (2016).
33. Roschger, A. *et al.* Differential accumulation of lead and zinc in double-tidemarks of articular cartilage. *Osteoarthritis Cartilage* **21**(11), 1707–1715. <https://doi.org/10.1016/j.joca.2013.06.029> (2013).
34. Zoeger, N. *et al.* Lead accumulation in tidemark of articular cartilage. *Osteoarthritis Cartilage* **14**(9), 906–913. <https://doi.org/10.1016/j.joca.2006.03.001> (2006).
35. Jin, Q. *et al.* Preserving elemental content in adherent mammalian cells for analysis by synchrotron-based X-ray fluorescence microscopy. *J. Microsc.* **265**(1), 81–93. <https://doi.org/10.1111/jmi.12466> (2017).
36. Hackett, M. J. *et al.* Chemical alterations to murine brain tissue induced by formalin fixation: Implications for biospectroscopic imaging and mapping studies of disease pathogenesis. *Analyst* **136**(14), 2941–2952. <https://doi.org/10.1039/c0an00269k> (2011).
37. Burkhart, K. J. *et al.* Influence of formalin fixation on the biomechanical properties of human diaphyseal bone. *Biomed. Tech.* **55**(6), 361–365. <https://doi.org/10.1515/bmt.2010.043> (2010).
38. Hammer, N. *et al.* Ethanol and formaldehyde fixation irreversibly alter bones' organic matrix. *J. Mech. Behav. Biomed. Mater.* **29**, 252–258. <https://doi.org/10.1016/j.jmbbm.2013.09.008> (2014).
39. Fan, X. *et al.* A technique for preparing undecalcified osteochondral fresh frozen sections for elemental mapping and understanding disease etiology. *Histochem. Cell Biol.* <https://doi.org/10.1007/s00418-022-02135-8> (2022).
40. Fan, X. *et al.* The deterioration of calcified cartilage integrity reflects the severity of osteoarthritis: A structural, molecular, and biochemical analysis. *FASEB J.* **36**(2), e22142. <https://doi.org/10.1096/fj.202101449R> (2022).
41. Simkin, P. A. Consider the tidemark. *J. Rheumatol.* **39**(5), 890–892. <https://doi.org/10.3899/jrheum.110942> (2012).
42. Aghajanian, P. & Mohan, S. The art of building bone: Emerging role of chondrocyte-to-osteoblast transdifferentiation in endochondral ossification. *Bone Res.* **6**, 19. <https://doi.org/10.1038/s41413-018-0021-z> (2018).
43. Suri, S. & Walsh, D. A. Osteochondral alterations in osteoarthritis. *Bone* **51**(2), 204–211. <https://doi.org/10.1016/j.bone.2011.10.010> (2012).
44. Fan, X., Wu, X., Crawford, R., Xiao, Y. & Prasad, I. Macro, micro, and molecular: Changes of the osteochondral interface in osteoarthritis development. *Front. Cell. Dev. Biol.* **9**, 659654. <https://doi.org/10.3389/fcell.2021.659654> (2021).
45. Nishi, Y. Zinc and growth. *J. Am. Coll. Nutr.* **15**(4), 340–344. <https://doi.org/10.1080/07315724.1996.10718608> (1996).
46. Ito, A. *et al.* Zinc-releasing calcium phosphate for stimulating bone formation. *Mater. Sci. Eng. C* **22**(1), 21–25. [https://doi.org/10.1016/S0928-4931\(02\)00108-X](https://doi.org/10.1016/S0928-4931(02)00108-X) (2002).
47. Erben, R. G. *et al.* Long-term marginal zinc supply is not detrimental to the skeleton of aged female rats. *J. Nutr.* **139**(4), 703–709. <https://doi.org/10.3945/jn.108.099077> (2009).
48. Finnilä, M. A. J. *et al.* Mineral crystal thickness in calcified cartilage and subchondral bone in healthy and osteoarthritic human knees. *J. Bone Miner. Res.* **37**(9), 1700–1710. <https://doi.org/10.1002/jbmr.4642> (2022).
49. Wen, C. Y. *et al.* Collagen fibril stiffening in osteoarthritic cartilage of human beings revealed by atomic force microscopy. *Osteoarthritis Cartilage* **20**(8), 916–922. <https://doi.org/10.1016/j.joca.2012.04.018> (2012).
50. Bigi, A. *et al.* Structure refinements of lead-substituted calcium hydroxyapatite by X-ray powder fitting. *Acta Crystallogr. B* **45**(3), 247–251 (1989).

51. Morgan, T. J. *et al.* Quantitative X-ray fluorescence analysis of biomass (switchgrass, corn stover, eucalyptus, beech, and pine wood) with a typical commercial multi-element method on a WD-XRF spectrometer. *Energy Fuels* **29**(3), 1669–1685. <https://doi.org/10.1021/ef502380x> (2015).
52. Furman, B. D. *et al.* Joint degeneration following closed intraarticular fracture in the mouse knee: A model of posttraumatic arthritis. *J. Orthop. Res.* **25**(5), 578–592. <https://doi.org/10.1002/jor.20331> (2007).
53. Kawamoto, T. & Kawamoto, K. Preparation of thin frozen sections from nonfixed and undecalcified hard tissues using Kawamoto's film method (2020). *Methods Mol. Biol.* **2230**, 259–281. https://doi.org/10.1007/978-1-0716-1028-2_15 (2021).
54. Kawamoto, T. & Kawamoto, K. Preparation of thin frozen sections from nonfixed and undecalcified hard tissues using Kawamoto's film method (2012). *Methods Mol. Biol.* **1130**, 149–164. https://doi.org/10.1007/978-1-62703-989-5_11 (2014).
55. Howard, D. L. *et al.* The XFM beamline at the Australian synchrotron. *J. Synchrotron Radiat.* **27**(Pt 5), 1447–1458. <https://doi.org/10.1107/s1600577520010152> (2020).
56. Ryan, C. G. *et al.* The maia detector and event mode. *Synchrotron Radiat. News* **31**(6), 21–27. <https://doi.org/10.1080/08940886.2018.1528430> (2018).
57. Ryan, C. G. & Jamieson, D. N. Dynamic analysis: On-line quantitative PIXE microanalysis and its use in overlap-resolved elemental mapping. *Nucl. Instrum. Methods Phys. Res. B* **77**(1), 203–214. [https://doi.org/10.1016/0168-583X\(93\)95545-G](https://doi.org/10.1016/0168-583X(93)95545-G) (1993).
58. Ryan, C. G. *et al.* Nuclear microprobe–synchrotron synergy: Towards integrated quantitative real-time elemental imaging using PIXE and SXRF. *Nucl. Instrum. Methods Phys. Res. B* **231**(1), 183–188. <https://doi.org/10.1016/j.nimb.2005.01.054> (2005).
59. Ghanbarian, B., Hunt, A. G., Ewing, R. P. & Sahimi, M. Tortuosity in porous media: A critical review. *Soil Sci. Soc. Am. J.* **77**(5), 1461–1477. <https://doi.org/10.2136/sssaj2012.0435> (2013).
60. Genoud, S. *et al.* Simultaneous structural and elemental nano-imaging of human brain tissue. *Chem. Sci.* **11**(33), 8919–8927. <https://doi.org/10.1039/d0sc02844d> (2020).

Acknowledgements

IP would like to acknowledge the Prince Charles Hospital Research Foundation (RF-01), the NHMRC Investigator grant fellowship (APP1176298) and EMCR grant from Centre for Biomedical Technologies (QUT). The authors would like to thank the CARF Histology lab in KG-Q for its contribution to the cryo-sample preparation. XF acknowledges QUT Postgraduate Research Award (QUTPRA) and QUT HDR Tuition Fee Sponsorship. The authors acknowledge the Central Analytical Research Facility (CARF) at the Queensland University of Technology. Part of this research was undertaken on the XFM beamline at the Australian Synchrotron, part of ANSTO.

Author contributions

Conception and design: X.F., I.P.; Collection and assembly of data: X.F., K.M.L., I.P., M.J., D.H.; Drafting of the article: X.F., I.P., M.J., R.C.; Critical revision of the article for important intellectual content: All authors; Obtain of funding: I.P.; All authors take responsibility for the integrity of the paper.

Competing interests

The authors declare no competing interests.

Additional information

Supplementary Information The online version contains supplementary material available at <https://doi.org/10.1038/s41598-023-36911-w>.

Correspondence and requests for materials should be addressed to I.P.

Reprints and permissions information is available at www.nature.com/reprints.

Publisher's note Springer Nature remains neutral with regard to jurisdictional claims in published maps and institutional affiliations.



Open Access This article is licensed under a Creative Commons Attribution 4.0 International License, which permits use, sharing, adaptation, distribution and reproduction in any medium or format, as long as you give appropriate credit to the original author(s) and the source, provide a link to the Creative Commons licence, and indicate if changes were made. The images or other third party material in this article are included in the article's Creative Commons licence, unless indicated otherwise in a credit line to the material. If material is not included in the article's Creative Commons licence and your intended use is not permitted by statutory regulation or exceeds the permitted use, you will need to obtain permission directly from the copyright holder. To view a copy of this licence, visit <http://creativecommons.org/licenses/by/4.0/>.

© The Author(s) 2023